Article

Fabrication of a Nickel Ferrite/Nanocellulose-Based Nanocomposite as an Active Sensing Material for the Detection of Chlorine Gas

Nurjahirah Janudin [1,*], Noor Azilah Mohd Kasim [1,2,*], Victor Feizal Knight [1,*], Mohd Nor Faiz Norrrahim [1], Mas Amira Idayu Abdul Razak [1], Norhana Abdul Halim [1,2], Siti Aminah Mohd Noor [1,2], Keat Khim Ong [1,2], Mohd Hanif Yaacob [3], Muhammad Zamharir Ahmad [4] and Wan Md Zin Wan Yunus [5]

[1] Research Centre for Chemical Defence, Universiti Pertahanan Nasional Malaysia, Kem Perdana Sungai Besi, Kuala Lumpur 57000, Malaysia; faiznorrrahim@gmail.com (M.N.F.N.); masamira920724@gmail.com (M.A.I.A.R.); norhana@upnm.edu.my (N.A.H.); s.aminah@upnm.edu.my (S.A.M.N.); ongkhim@upnm.edu.my (K.K.O.)

[2] Centre for Defence Foundation Studies, Department of Chemistry and Biology, Universiti Pertahanan Nasional Malaysia, Kem Perdana Sungai Besi, Kuala Lumpur 57000, Malaysia

[3] Wireless and Photonic Research Centre (WiPNET), Faculty of Engineering, Universiti Putra Malaysia, Serdang 43400, Malaysia; hanif@upm.edu.my

[4] Malaysia Agricultural Research and Development Institute, Lot PT3747, Jalan Tambun Tulang, Arau 02600, Malaysia; zamharir@mardi.gov.my

[5] Centre for Tropicalisation, Universiti Pertahanan Nasional Malaysia, Kem Perdana Sungai Besi, Kuala Lumpur 57000, Malaysia; wanmdzin@upnm.edu.my

* Correspondence: nurjahirahjanudin@gmail.com (N.J.); azilah@upnm.edu.my (N.A.M.K.); victor.feizal@upnm.edu.my (V.F.K.)

Abstract: Chlorine gas is extensively utilised in industries as both a disinfectant and for wastewater treatment. It has a pungent and irritating odour that is comparable with that of bleach and can cause serious health issues such as headaches and breathing difficulties. Hence, efficiently, and accurately monitoring chlorine gas is critical to ensure that no undesirable incidents occur. Due to its remarkable characteristics, numerous researchers have explored the potential of ferrite nanoparticles as a sensing material for chlorine gas detection. Among several ferrite nanoparticles, nickel ferrite ($NiFe_2O_4$) is extensively studied as an inverse spinel structured magnetic material that may be ideal for sensing applications. However, the magnetic characteristics of $NiFe_2O_4$ cause agglomeration, which necessitates the use of a substrate for stabilisation. Therefore, nanocellulose (NC), as a green and eco-friendly substrate, is ideal for stabilising bare nickel ferrite nanoparticles. In a novel experiment, nickel ferrite was loaded onto NC as a substrate using in situ deposition. The structure was confirmed by X-ray Diffraction (XRD) analysis, while elemental composition was verified by Energy dispersive X-ray (EDX) analysis. Gas sensing properties were determined by evaluating sensitivity as a function of various regulating factors, such as the amount of nickel ferrite, gas concentration, repeatability, and reusability. In the evaluation, 0.3 g nickel ferrite showed superior response and sensitivity than those of other samples. The achieved response time was around 40 s, while recovery time was about 50 s. This study demonstrates the potential of a nickel ferrite/nanocellulose-based nanocomposite to efficiently monitor chlorine gas.

Keywords: nickel ferrite; nanocellulose; chlorine gas; magnetic material; sensor

1. Introduction

Gases such as ammonia, benzene, carbon dioxide, hydrogen sulphide, carbon monoxide, and chlorine are readily available and can cause serious health concerns when they are present in the environment without being safely contained [1–5]. Chlorine is widely used in a variety of applications in both household and industrial environments, including its use as a disinfecting agent in swimming pools and drinking water to kill harmful pathogens [6],

as bleach in the manufacture of fabrics, paper products, insecticides, rubber products, and solvents [7–12]. In fact, when chlorinated bleach is combined with certain cleaning products, it can form chlorine gas. Furthermore, during World War I, chlorine gained notoriety when it was utilised as a chemical warfare agent (CWA), and it has since been classified as a CWA choking agent. Chlorine gas is yellowish green and is often delivered under pressure and kept in liquid form. It is recognised by its strong and irritating odour, which provides early warning to those who become exposed to it. While it is not flammable, it may react explosively with other chemicals such as turpentine and ammonia to produce explosive compounds such as chloramine.

Chlorine overexposure can cause a variety of health issues such as blurred vision, coughing, troubled breathing, nausea, vomiting, watery eyes, wheezing, and skin blisters should it encounter the skin. It can induce toxic pneumonitis and severe pulmonary oedema if exposure is between 40 and 60 ppm, and it can be deadly within 30 min of exposure if exposure is above 400 ppm [13]. The immediately dangerous to life and health (IDLH) concentration of chlorine is 10 ppm, while the occupational exposure limit (OEL) is 0.5 ppm. It is not just chlorine gas that can cause respiratory toxicity; other chlorine-containing compounds such as hypochlorous acid, chlorine dioxide, and chloramine can all cause the same symptoms and signs as chlorine gas does [14]. Repeated exposure to chlorine in swimming pools may also be a substantial risk factor for swimmers to develop asthma. Therefore, it is critical to develop suitable chlorine sensors that are both extremely sensitive and selective for use in real-time monitoring.

Semiconductor metal oxide sensors such as tin oxide (SnO_2), zinc oxide (ZnO_2), and tungsten oxide (WO_3) are frequently used as gas sensors [15–20]; nevertheless, they require significant power because of their need to operate at high elevated temperatures and also have general selectivity issues. Hence, there is a continuing need for the development of novel gas-sensor material. Apart from magnetic and electrical applications, ferrites are studied for gas- and humidity-sensing applications [21–24]. Nickel ferrite nanoparticles are useful gas sensors for different gases, such as carbon monoxide (CO), hydrogen disulphide (H_2S), and chlorine (Cl_2), and for liquified petroleum gas (LPG) [25–27]. However, nickel ferrite nanoparticles as gas sensors receive less attention. Nanoparticles have an efficacious grain size that provides a voluminous surface area to promote the adsorption of numerous gases [28]. The use of nanoparticles in thin-film sensors enhances the sensitivity and performance of gas sensors. Thin-film sensors provide certain advantages such as a high surface-area-to-volume ratio, which improves the interaction between gas analyte and sensing material; lower energy input; low power consumption; compactness; and overall cost efficiency. Consequently, the sensitivity and selectivity of gas sensors using this material are enhanced. As shown in Figure 1, a search on lens.org using the keyword 'metal-oxide-based gas sensor' revealed that publications focusing on metal oxides as sensing material have increased in recent years. Therefore, research on metal oxides as gas sensors continues to pique the interest of scientists.

Metal oxide sensing mechanisms are mostly dependent on charge transfer mechanisms, which include oxygen and target analytes (see Figure 2). When the sensing material is operated at temperatures above 150 °C, oxygen molecules from the air chemisorb onto the sensing material's surface, thus capturing electrons and transforming them into O_2^-, O^-, or O^{2-}. When the sensing material is operated at room temperature, the opposite trend occurs. As an electrical charge carrier, the majority carrier is a hole, and the target analyte chemisorbs onto the sensing material's surface, reducing the concentration of holes, thereby increasing the sensing material's resistivity [29]. Available papers that report on the efficient gas sensing performance of nickel ferrite nanoparticles are listed in Table 1.
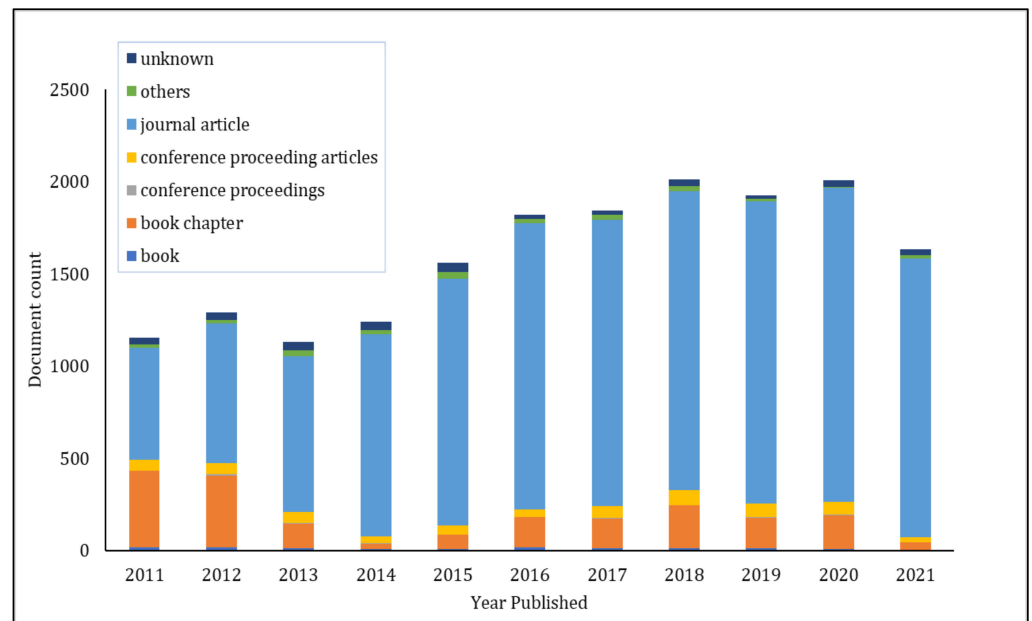
Figure 1. Bar chart of published manuscripts focusing on metal-oxide-based gas sensors.
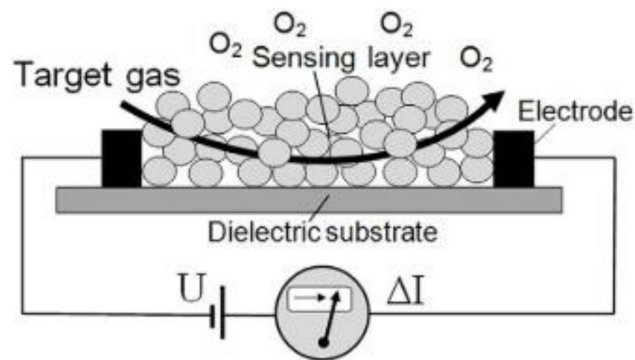

Figure 2. Schematic diagram of metal oxide sensing mechanism [30].

Table 1. Reports of efficient gas-sensing performance of nickel ferrite nanoparticles.

Sensing Material	Target Gas	Operating T (°C)	Concentration of Gas (ppm)	R_T and R_C	S (%)	Ref.
Pd-doped $NiFe_2O_4$	Cl_2	325	15	2 s and 6 s	6.9	[31]
Co-doped $NiFe_2O_4$	LPG	250	5000	25 s and 240 s	86	[32]
Li-doped $NiFe_2O_4$	H_2	200	100	Not mentioned	1.09	[33]
Nb_2O_5 mixed with $NiFe_2O_4$	Humidity	25	11–97 %	20 s and 30 s	1190	[34]
$Ru-NiFe_2O_4$	H_2	100	50	Not mentioned	1.36	[35]
$NiFe_2O_4$	Triethylamine	190	50	6 s and 585 s	18.9	[36]

T: temperature; R_T: response time; R_C: recovery time; S: sensitivity.

On the other hand, nickel ferrite has the major drawback of tending to agglomerate as a result of its magnetic characteristics, which then impacts its physical characteristics. This necessitates further treatment of ferrite nanoparticles in order to increase their dispersibility. Virlan et al. (2017) demonstrated that heat treatments improved the sensibility of their sensing material. The morphology of mixed Co−Ni ferrites is affected by calcination temperatures, but it has no effect on their magnetic characteristics. The porosity and specific surface area of the material were enhanced, thus improving their sensibility and specificity as a sensor [37]. Ferrite nanoparticles with cellulose nanocrystals (CNC) were modified by

Lizundia et al. (2020). They successful fabricated a well-dispersed hybrid material with both magnetic and conductive properties using CNC processes that kept the material homogeneously distributed at the molecular level [38]. Gupta et al. (2017) revealed that the catalytic activity of nanocellulose-nickel ferrite nanocomposites was enhanced due to stabilisation and increased the dispersibility of $NiFe_2O_4$ nanoparticles in a cellulose matrix [39]. Nanocellulose, as an eco-friendly material, can be incorporated with ferrite nanoparticles, thus obtaining organic–inorganic hybrid composites with upgraded functional characteristics. This is due to the presence of hydroxyl groups on the surface of nanocellulose and the interaction of van der Waals forces [40,41] contributing to the attachment of inorganic particles onto the nanocellulose. Furthermore, nanocellulose has a high surface area, a unique morphology, strong mechanical characteristics, and nanoscale dimensions [42,43], thus rendering it an ideal template for stabilising bare ferrite nanoparticles.

In view of these developments, we attempted to synthesise nickel ferrite loaded onto nanocellulose using an in-situ preparation technique. The nickel ferrite was loaded using different amounts to optimise their sensing characteristics. The structure was examined using XRD analysis, and its elemental composition was evaluated using EDX analysis. Sensing measurements towards chlorine gas were carried out using a fabricated thin-film sensor in a customised test chamber in ambient conditions. The gas concentration, sensitivity, repeatability, and reusability of the sensing material were explored. The combination of structural stability, high surface area, and nickel ferrite and nanocellulose being a well-dispersed composite is an excellent sensing material with vast potential applicability in numerous fields such as biomedicine, wastewater treatment, industrial applications, and for household monitoring.

2. Materials and Methods

2.1. Materials

Nickel ferrite ($NiFe_2O_4$) was purchased from Alfa (New York, NY, USA). Nanocellulose/cellulose nanofibrilled in water suspension (2% *w/v*) was obtained from Zoepnano Sdn. Bhd (Selangor, Malaysia). Liquor ammonia, ethanol, and silver conductive paste were acquired from Merck (Kenilworth, NJ, USA) and used without any pretreatment. A gold ribbon with a thickness of 0.01 mm was purchased from Coining, Ametek (Montvale, NJ, USA).

2.2. Nanocomposite Preparation

Nanocellulose was suspended in distilled water and sonicated for 15 min to break up any fibre agglomerations. Then, 0.1 g of nickel ferrite was dissolved in 10 mL distilled water. Drop by drop, the prepared nickel ferrite salt solution was added to the 0.1 g nanocellulose suspension. By adding liquor ammonia, the pH of the solution was adjusted to 7.5, and stirring continued for 2 h. After the reaction had been completed, the nanocellulose–nickel ferrite solution was filtered through a 0.45 μm thick cellulose nitrate membrane filter and rinsed multiple times with distilled water. The end product was dried for 24 h in a vacuum oven at 70 °C. To evaluate the effects of loading different amounts of nickel ferrite towards sensing characteristics, the concentrations of the nickel ferrite solution were varied: 0.1, 0.2, 0.3, 0.4, and 0.5 g. A schematic diagram of the preparation of the nanocomposite is shown in Figure 3.
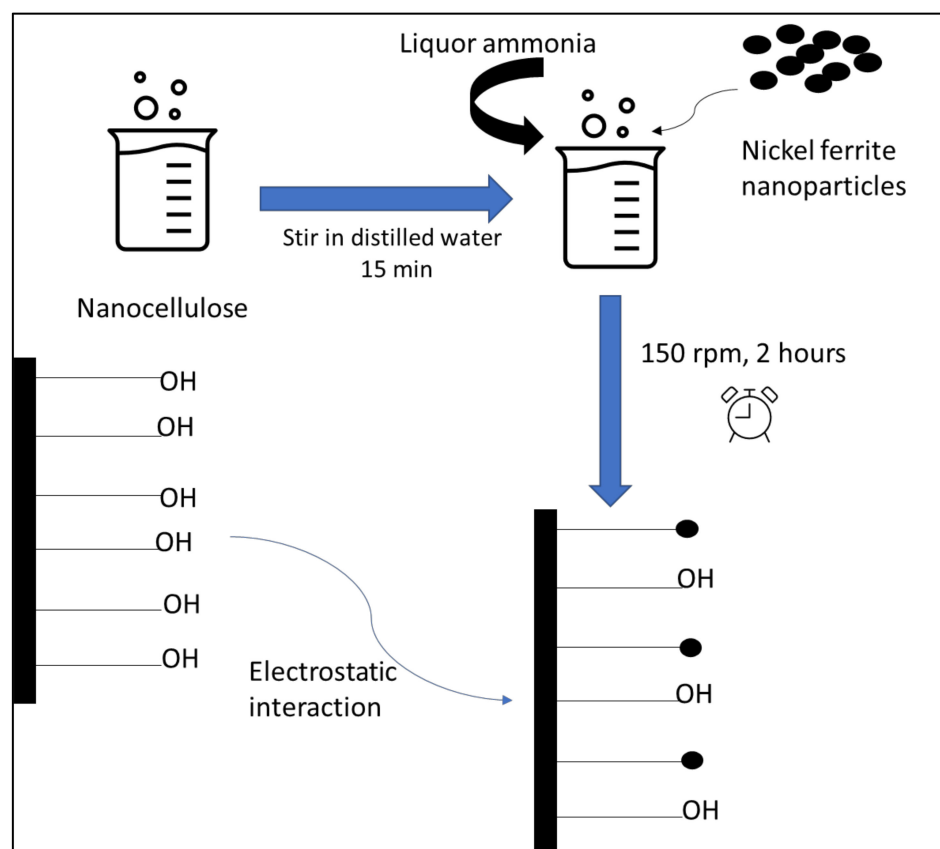
Figure 3. Schematic diagram of preparation nanocomposite.

2.3. Characterisation of Hybrid Nanocomposites

2.3.1. X-ray Diffraction Analysis

X-Ray diffraction analysis (XRD) is a non-destructive method used to identify the crystalline structure of samples. XRD patterns of the nanocellulose, nickel ferrite, and nanocellulose-nickel ferrite nanocomposites were recorded using a Smart APEX II Bruker AXS GmbH (Karlsruhe, Germany), and Bragg's scanning angle varied from 10° to 90°. Samples were examined at ambient temperature with Cu–Kα radiation (wavelength 1.54 Å). Data analysis began with the subtraction of a blank run to remove the environmental background before sample crystallinity was analysed.

2.3.2. Energy-Dispersive X-ray Analysis

Energy-dispersive X-ray (EDX) is a technique used to examine the elemental composition of a sample. EDX analysis was integrated in a Zeiss Gemini500 SEM instrument (Jena, Germany). Elemental composition presence in the nanocomposites is presented in the form of percentages. Nickel and iron elements appeared as indications of the attached nickel ferrite.

2.4. Sensing Measurements

2.4.1. Preparation of Thin-Film Sensing Materials

Ethanol was used to clean a prepatterned gold (Au) interdigitated transducer (IDT) with a 50 μm line/space. The IDT was then annealed in an oven for 15 min at 50 °C to evaporate any remaining solvent. Using the silver conductive paste, a gold ribbon (99.9% purity) was placed onto the gold (Au) pads and allowed to dry and harden under a heated environment of 60 °C for 15 min. Approximately 2.5 μL of the hybrid nanocomposite solution was then drop-cast onto the IDT using an Eppendorf micropipette. The prepared

IDT was then dried at room temperature for 24 h. The same technique was used to prepare the pristine nanocellulose and bare nickel ferrite IDTs as controls in the experiment.

2.4.2. Detection of Chlorine Gas

As is shown in Figure 4, IDTs loaded with the nanocomposites were installed in a designed gas test chamber and attached to a digital multimeter and temperature controller. The digital multimeter was connected to a computer running FlukeView form software to record the samples' electrical resistance changes in real time. The gas test chamber was integrated into a gas calibration system that included a computer-controlled mass flow controller that regulated gas flow at 200 standard cubic centimetres per minute (sccm). The concentration of chlorine gas was changed by regulating the dilution of 1% chlorine gas with an inert carrier gas, in this case, nitrogen. The resistance was then continuously measured while the sample was subjected to various concentrations of chlorine gas. The dynamic response obtained from each of the sample IDTs was observed as a change in resistance when the test chamber was alternately filled and purged with chlorine and nitrogen gas. Measurements were taken at ambient temperature and in a constant humidified atmosphere (55%). Equation (1) was used to calculate the sensitivity of the sensing material:

$$S = \frac{\Delta R}{R_o} = \frac{R_g - R_o}{R_o} \times 100\% \tag{1}$$

where S denotes the sensitivity of the sensing material, R_g denotes the resistance of the sample upon exposure to chlorine gas, and R_o denotes resistance in the sample upon exposure to nitrogen gas.
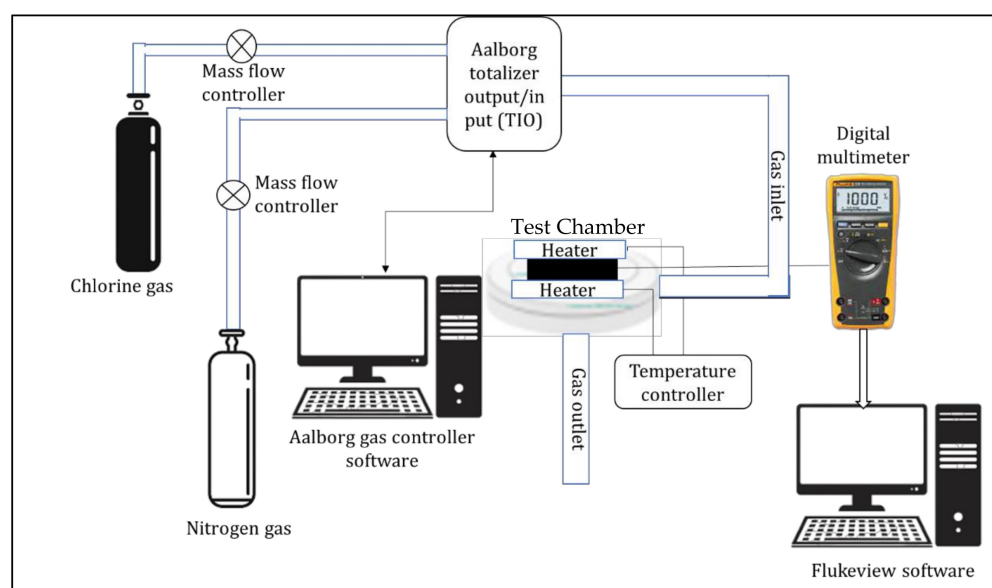
Figure 4. Sensor test setup.

The repeatability study was conducted using the same material at optimal concentrations and injected with 1% chlorine. The reusability study was conducted using the same material at optimal concentrations, but in five different days. The change in resistance was measured using the same calculation as above.

3. Results and Discussion

3.1. Characterisation

Figure 5 displays the X-ray diffraction patterns of nanocellulose, nickel ferrite, and the hybrid nanocomposites comprising five different NC weight loading levels (0.1, 0.2, 0.3, 0.4, and 0.5 g). All peaks were prominent, and matched well with JCPDS card no.

00-050-2241 and JCPDS card no. 10-0325, which indicated the crystalline structure of the pristine nanocellulose and the spinel cubic structure of pure nickel ferrite nanoparticles. The XRD diffraction pattern showed peaks around $2\theta = 17.69°$ (101), $22.08°$ (002) and $34.51°$ (040), which indicated a typical cellulose structure [39]. The matched scan data of $NiFe_2O_4$ showed the formation of crystalline nickel ferrite nanoparticles, as indicated in JCPDS card no. 00-003-0875. Obtained diffraction patterns were $31.01°$, $35.99°$, $43.72°$, $54.49°$, $57.89°$, $63.27°$, and $75.05°$, which were assigned to the reflection of planes (220), (311), (400), (422), (511), (440), and (620), respectively [28]. We did not observe any extra peaks that could indicate the presence of any impurities in the prepared sample, thereby confirming the purity of the sample. In the XRD pattern of the nanocomposites, besides typical peaks of nanocellulose at $2\theta = 22.73°$ (002), there were some other diffraction peaks that matched well with the standard pattern of $NiFe_2O_4$. As the concentration of nickel ferrite increased, peaks corresponding to $NiFe_2O_4$ became prominent and intense, while peaks corresponding to nanocellulose decreased in intensity, as is shown in Figure 5. Crystallite size was calculated from the line broadening of the most intense (0 0 2) and (3 1 1) peaks of nanocellulose and nickel ferrite using the Scherrer equation [44]. In X-ray diffraction and crystallography, the Scherrer equation is a formula that relates the size of submicrometric crystallites in a solid to the broadening of a peak in a diffraction pattern. Equation (2) shows the modified Scherrer equation formula [45]. Bragg's equation was used to calculate lattice parameters. The values of the lattice parameter were in the range of 8.1810–8.2690. The values of crystallite size and lattice parameters of nanocellulose and its composites with nickel ferrite are shown in Table 2.

$$D = \frac{\lambda}{3\beta \cos\theta} \qquad (2)$$

where 1/3 is the correction value of shape factor K in the Scherrer equation; λ is the X-ray radiation wavelength; β and θ are the full-width half maximum and the half of the diffraction angle (2θ), respectively, at the crystal planes detected in the XRD spectrum.
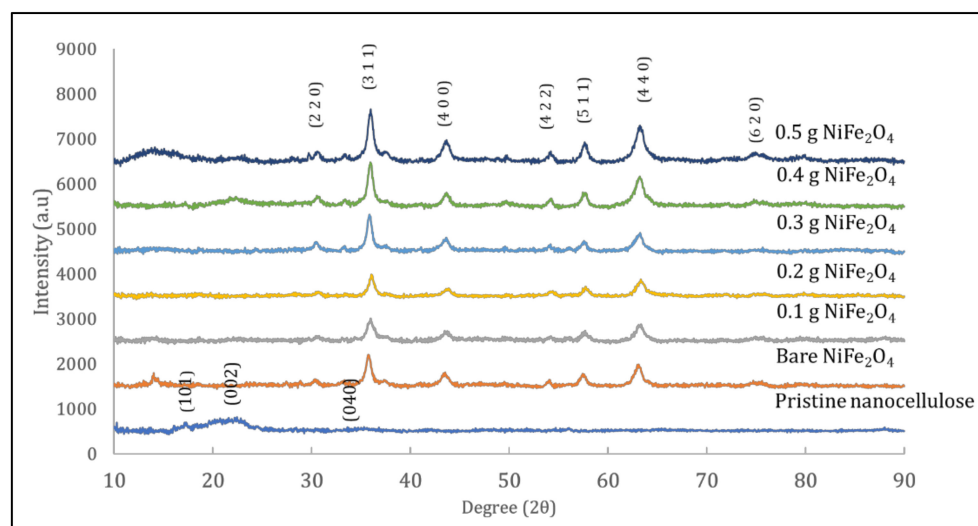

Figure 5. XRD pattern of pristine nanocellulose, bare $NiFe_2O_4$, and hybrid nanocomposites.

Samples were then examined using energy-dispersive X-ray spectroscopy analysis (EDX) to evaluate the ratio between divalent cations contained in the nanoparticles to further validate the occurrence of mixed ferrites. The elemental composition of pristine nanocellulose and bare nickel ferrite is shown in Figure 6a. Findings revealed that nanocellulose contained carbon, oxygen, hydrogen, and a small number of impurities (not shown in the graph). Impurities were most likely due to sulphuric acid from the production process [46]. Figure 6a also confirms the purity of nickel ferrite through the presence of Ni, Fe,

and O elements, which agreed well with the theoretical values (Fe: 48.97%, Ni: 24.42%, and O: 29.61%) [47]. The hybrid nanocomposites possessed material compositions that were similar to the desired ratios, as shown in Figure 6b. Minor differences could be attributed to technical errors, but overall results indicated the production of tertiary ferrites with well-defined composition. EDX results also corresponded well with lattice parameters estimated from XRD data, thus doubly validating the composition of the nanocomposites [48]. Ferrite ions were successfully diffused and adsorbed onto the nanocellulose surface when the nickel ferrite was submerged in a mixture of nanocellulose solutions via electrostatic interactions. Upon the addition of liquor ammonia, the basic hydrolysis of ferrite ions occurred, inducing a nickel ferrite nanoparticle colloidal solution to form, and the solution darkened as a result of the production of the nickel ferrite nanoparticles. The suspension was well-dispersed and stable because of the strong interactions between nickel ferrite and nanocellulose [39].

Table 2. Lattice parameters and average crystallite size of nickel ferrite nanocellulose.

| Sample	Lattice Parameters (Å)	Average Crystallite Size, D (nm)	
		Nanocellulose	NiFe$_2$O$_4$
Pristine NC	—	1.40	—
Bare NiFe$_2$O$_4$	8.2690	—	0.83
NC + 0.1 g NiFe$_2$O$_4$	8.1810	1.34	0.96
NC + 0.2 g NiFe$_2$O$_4$	8.2010	1.28	0.97
NC + 0.3 g NiFe$_2$O$_4$	8.2125	1.22	0.98
NC + 0.4 g NiFe$_2$O$_4$	8.2183	1.33	0.83
NC + 0.5 g NiFe$_2$O$_4$	8.2203	1.25	0.93
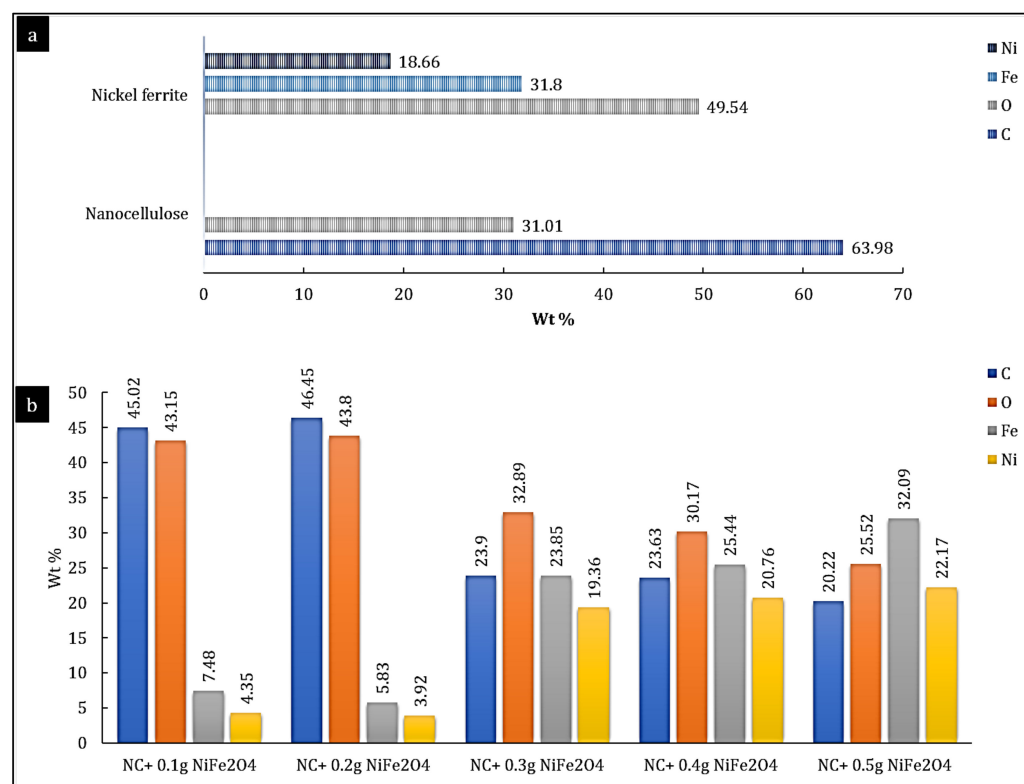
Figure 6. Elemental composition of (**a**) nanocellulose and nickel ferrite (**b**) hybrid nanocomposites.

3.2. Sensing Characteristics

3.2.1. Pristine Nanocellulose and Nickel Ferrite

Sensing characteristics of the hybrid nanocomposites as a thin-film sensor were studied by exposing them to chlorine gas at ambient temperature. In the control experiment, a sample without any hybrid nanocomposites was placed in the customised test chamber to evaluate any differences in the responses of a pristine sample and the hybrid nanocomposites. Responses for pure nanocellulose and nickel ferrite nanoparticles are both shown in Figure 7. The thin-film sensor's resistance was initially examined in a nitrogen atmosphere before the introduction of any other gas into the customised test chamber. The chamber was then filled with 1% chlorine gas. The response of the nanocellulose-based thin film sensor was significantly lower due to the weak conductivity of the nanocellulose. On the other hand, the nickel ferrite nanoparticle thin-film sensor sample exhibited increased resistance as its sensor response. As nickel ferrite is highly conductive, it can promptly respond to the presence of target analytes. After the chlorine gas in the test chamber had reached a steady state, it was purged from the chamber by introducing nitrogen gas. The thin-film sensor's baseline recovered within several minutes after the evacuation of chlorine gas from the test chamber, indicating that the nickel ferrite nanoparticles displayed a recovery phase within a short span of time. After these control experiments had been completed, hybrid nanocomposites were placed in the customised test chamber to analyse their sensing capabilities.
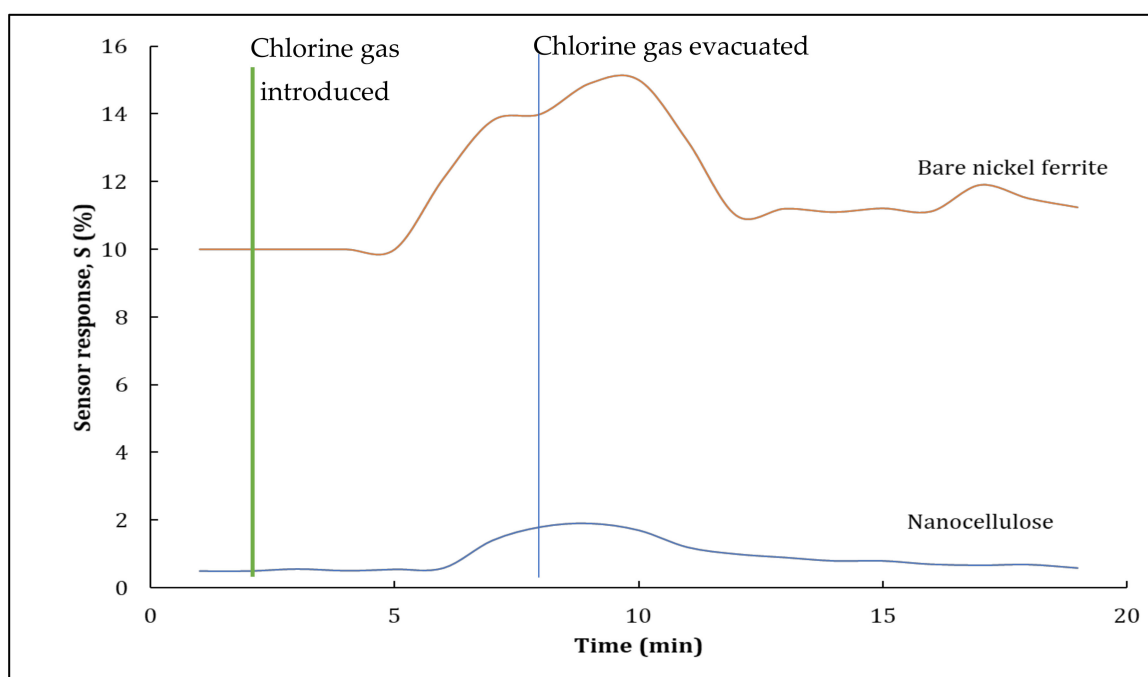

Figure 7. Sensor response of pristine nanocellulose and bare nickel ferrite.

3.2.2. Nickel ferrite–nanocellulose nanocomposites

The responses of the different quantities of nickel ferrite samples deposited onto the nanocellulose are represented in Figure 8. The magnetic characteristics of ferrite particles were stabilised by using nanocellulose as a substrate. Upon the introduction of chlorine gas into the test chamber, all samples demonstrated a good response. When the sensing materials were exposed to chlorine gas, the chlorine attracted electrons from the sensing materials, thus increasing their electrical resistance. When the chlorine gas was withdrawn, the reaction reversed. Trapped electrons returned to the sensing material, thus increasing the density of electrons in the material, and this lead to a decrease in electrical resistance. The basic mechanism of semiconductor metal oxides is based on charge transfer. The behaviour in this experiment indicated that the sample was a *p*-type semiconductor, this

being a majority carrier of holes. In a *p*-type semiconductor, the tested gas draws electrons from the sensing material and thus increases the concentration of holes, resulting in an increase in resistance [49].
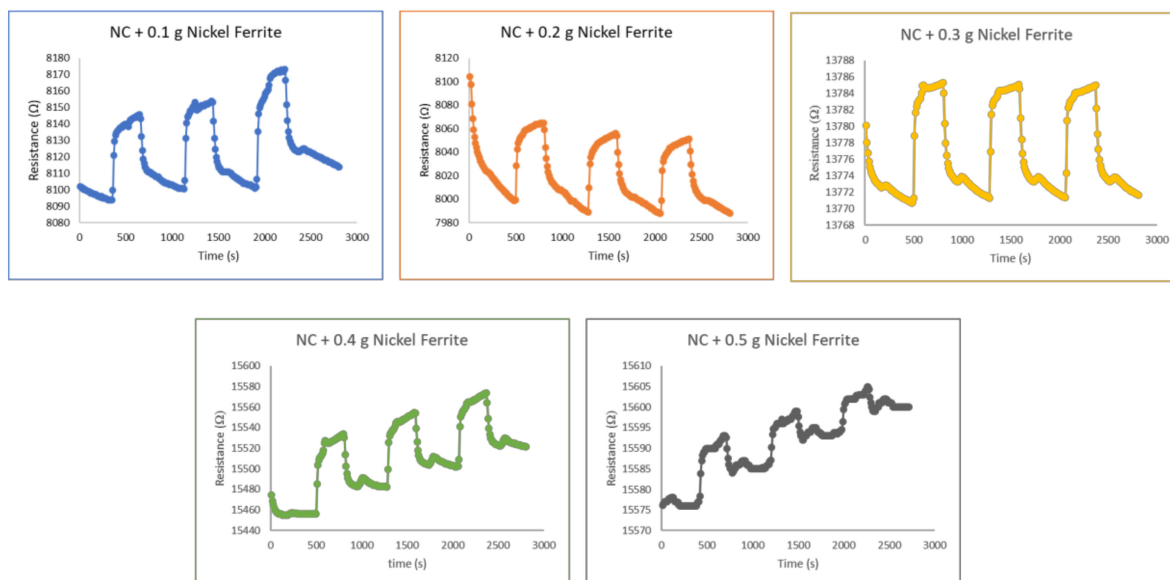

Figure 8. Response of nickel ferrite–nanocellulose nanocomposites to 1% chlorine gas.

Since Cl_2 gas detection is a surface phenomenon, the number of accessible active sites on the surface of a sensor is critical in determining the effectiveness of the sensing material. However, this experiment revealed that the samples were unable to immediately recover to their baseline resistance value. This was very likely due to the tested gas being chemisorbed onto the surface of the sensing medium. The adsorption of gas analytes onto sensing materials can be classified into two types: physisorption and chemisorption. Physisorption occurs when the molecular interaction occurring is mostly driven by van der Waals forces, whereas chemisorption happens when valence forces such as those found in the formation of chemical pollutants are involved. Both adsorption processes can occur on the same surface and are influenced by any increases in surface area [50]. The interaction between gas analyte and sensing material in our situation was most likely chemisorption, which then resulted in the samples having difficulty in recovering their baseline resistance values. This could be remediated through the use of heat treatment or UV illumination to facilitate electron release from the sensing material. The baseline could not be recovered in this experiment, probably because active sites on the sensing material continued to be saturated with the gas analyte and were difficult to remove. In a similar experiment, Sharma et al. (2018) described a similar phenomenon in which a chlorine sensor based on carbon nanotubes modified with hexadecafluorinated copper phthalocyanine failed to regain its baseline resistance, even after a long period of time. Nonetheless, they found that adding heat to the sensing materials greatly enhanced the material's recovery properties [51].

3.2.3. Sensitivity Study of Hybrid Nanocomposites

Figure 9a illustrates the sensitivity of a hybrid nanocomposite after being exposed to 1% chlorine gas. With respect to the nickel ferrite, the use of different amounts, namely, 0.1, 0.2, 0.3, 0.4, and 0.5 g produced sensitivities of 0.04%, 0.05%, 0.7%, 0.08%, and 0.05%, respectively. Nickel ferrite has outstanding sensing properties, such as great conductivity, high surface area, and the presence of two different cation sites. Combining cations in the ferrite particles opens up the possibility of designing promising sensing materials with improved sensitivity, selectivity, responsiveness, and long-term stability [52]. Furthermore, nickel ferrite has a lower reaction barrier compared to that of other metals (see Table 3), which renders them highly

effective at dissociating chlorine molecules, resulting in a rapid response to the presence of chlorine gas. Increasing the quantity of nickel ferrite promotes an increased number of active sites for Cl_2 gas adsorption on the surface of the sensing material. The deposition of nickel ferrite onto nanocellulose is expected to enhance their dispersibility in the material. Thus, well-dispersed ferrite nanoparticles on the surface of nanocellulose would enable extensive contact with gas analytes, thereby increasing the sensing material's sensitivity. However, once the concentration of nickel ferrite exceeded 0.3 g, sensitivity was reduced. This was likely because nickel ferrite tends to agglomerate on surfaces. This agglomeration limits interactions between gas analytes and the sensing material, hence resulting in reduced sensitivity. Rao et al. (2016) reported that nickel ferrite doped with palladium in a thin-film Cl_2 sensor had a sensitivity of 6.9 at a working temperature of 325 °C [31]. Zhang et al. (2019) utilised a three-dimensional open porous tin dioxide (SnO_2) chlorine sensor with a high sensitivity of 792.85 to 5 ppm Cl_2 at 160 °C [53]. Even though the sensitivity of 0.3 g nickel ferrite coated onto nanocellulose had a significantly lower value (0.7), the needed operating temperature was room temperature, which indicated that minimal maintenance would be needed, and there would be lower manufacturing costs in a room-temperature sensor device for chlorine monitoring applications.
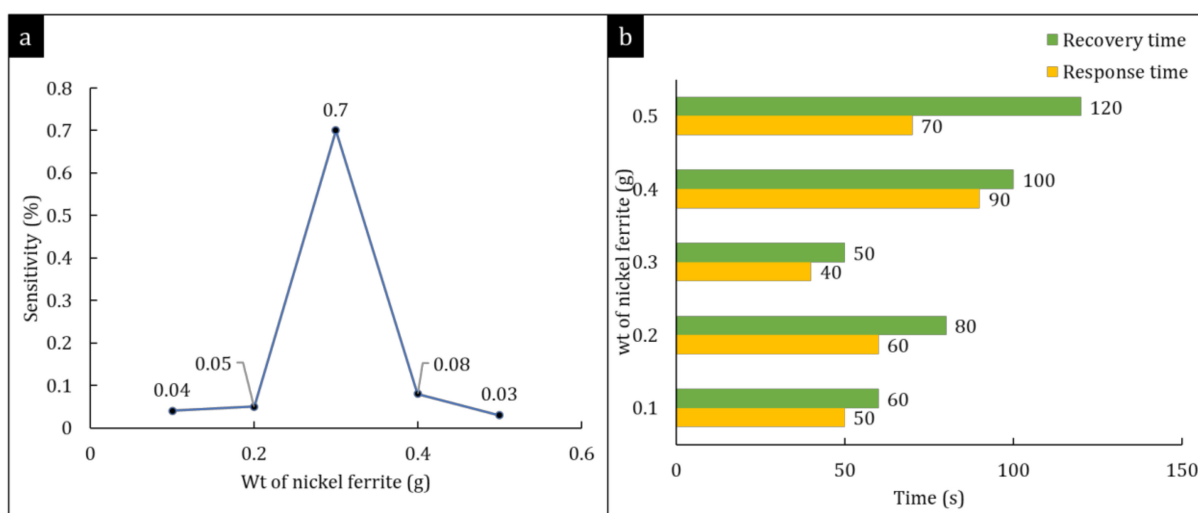

Figure 9. (**a**) Sensitivity of different amounts of nickel ferrite towards chlorine gas. (**b**) Response and recovery time of different hybrid nanocomposites.

In effective gas sensors, response and recovery characteristics are important criteria to be considered. When a sensor is exposed to gas, its response time is defined as the time taken for the sensor to achieve 90% of the entire current/resistance/voltage change, and recovery time is the time that it takes to remove the gas from the sensor. In our study, 0.3 g of nickel ferrite demonstrated promising response and recovery times of 40 and 50 s, respectively. Hybrid nanocomposite samples showed varying response times, from 50 to 90 s, and recovery times from 60 to 120 s (Figure 9b). The 0.3 g nickel ferrite thin film had the fastest reaction time and recovery time, suggesting that it would be a better sensor. Bedi et al. (2010) reported that their copper (II) 1,4,8,11,15,18,22,25-octabutoxy-29H,31H-phthalocyanine thin film as a Cl_2 gas sensor that could operate at room temperature with high sensitivity (185%), but it had a response time of 9.5 min. The sensor also needed to be heated to 195 °C in order to achieve recovery [54]. High sensitivity (50%) could also be obtained using $NiZnFe_2O_4$ to detect 1000 ppm Cl_2 at room temperature, but response and recovery times were much longer (10 and 13 min, respectively) [44] than those found in this study.

Table 3. Metal reaction barrier.

Metal Oxides	Reaction Barrier	Ref.
Metal atoms (X = Cu, Zn, Cd, Ga, Al, Au, or Hg) with YH_4 molecules (Y = C, Si, or Ge)	85–109.8	[55]
Ga-21.5In-10Sn/Cu	98–106.7	[56]
$MgCl_2$	290.2	[57]
$NiFe_2O_4$	~7	[58]

Figure 10 depicts the different hybrid nanocomposite responses as a function of gas concentration. The sensitivity of these different hybrid nanocomposites was compared at 25 °C. The sensor response of the nickel ferrite–nanocellulose nanocomposites was about 0.24%, 0.35%, 0.48%, 0.71%, and 0.90% for 0.3 g nickel ferrite loaded nanocomposite when exposed to Cl_2 gas concentrations of 0.125%, 0.25%, 0.5%, 0.75%, and 1.0%, respectively. The sensor response of the other hybrid nanocomposites, their fitting function, and the correlation coefficients of the fitted data are shown in Table 4. These observations revealed that there was a comparative increase in sensor response with increasing gas concentrations. The gas detection mechanism of a metal oxide semiconductor to a reducing gas (Cl_2) is described as follows. When the sensing material is exposed to a targeted gas, resistance changes depend on the interaction between gas analyte and sensing material. The adsorption of the gas analyte on the sensing material can influence response characteristics. A better response might be predicted when a substantial amount of gas analyte is adsorbed, increasing the sensitivity of the sensing material [59]. Hence, increases in sensor response as gas concentration increases are attributable to the presence of active sites on the sensing material. When larger amounts of gas analytes react at the active sites, this improves the adsorption of the gas, thus increasing the sensor response.
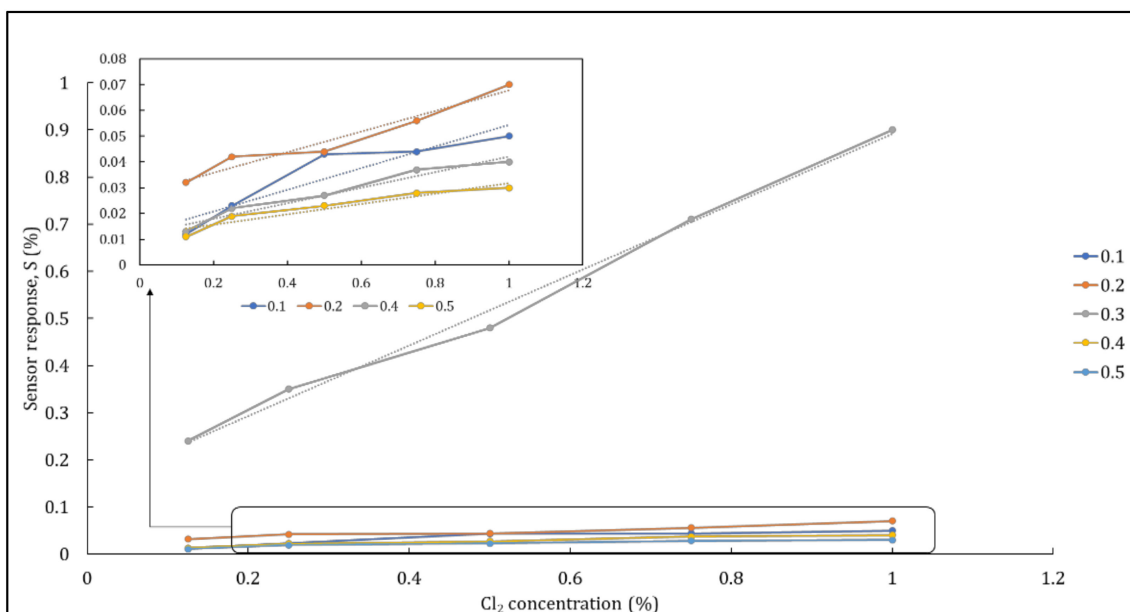

Figure 10. Sensor response of nickel ferrite–nanocellulose nanocomposite towards different chlorine concentrations.

Table 4. Sensor response, fitting function, and correlation coefficients (R^2) of nickel ferrite–nanocellulose nanocomposites.

Hybrid Nanocomposite	Concentration (%)					Fitting Function	R^2
	0.125	0.25	0.5	0.75	1.0		
NC + 0.1 g NiFe$_2$O$_4$	0.012	0.023	0.043	0.044	0.05	y = 0.0419x + 0.0124	0.8622
NC + 0.2 g NiFe$_2$O$_4$	0.032	0.042	0.044	0.056	0.07	y = 0.0398x + 0.0279	0.9522
NC + 0.3 g NiFe$_2$O$_4$	0.240	0.350	0.480	0.710	0.90	y = 0.7473x + 0.1437	0.9934
NC + 0.4 g NiFe$_2$O$_4$	0.013	0.022	0.027	0.037	0.04	y = 0.0300x + 0.012	0.9506
NC + 0.5 g NiFe$_2$O$_4$	0.011	0.019	0.023	0.028	0.03	y = 0.0202x + 0.0116	0.9056

3.2.4. Repeatability and Reusability of Hybrid Nanocomposites

Figure 11 exhibits the repeatability and reusability characteristics of the sensing material, which were examined using 0.3 g of nickel ferrite deposited onto the nanocellulose. The sensing material was exposed to 1.0% Cl$_2$ gas for five times in order to examine its repeatability, and the same sensing material was then exposed to a fixed concentration of Cl$_2$ gas over five consecutive days to examine its reusability. The sensing material was flushed with nitrogen gas to recover its baseline resistance value without any exposure to any form of heat treatment. The sensing material demonstrated good repeatability and reusability through not exhibiting any significant decrease in sensing performance throughout the tests. However, possibly due to a small amount of the gas analyte thoroughly penetrating the surface of the ferrite nanoparticles, there was a minor difference in the resistance value during the recovery phase, which may prove to be negligible. This finding indicates that the nickel ferrite–nanocellulose nanocomposite has considerable potential as a sensing material for monitoring hazardous gases, with good stability and recovery after exposure.
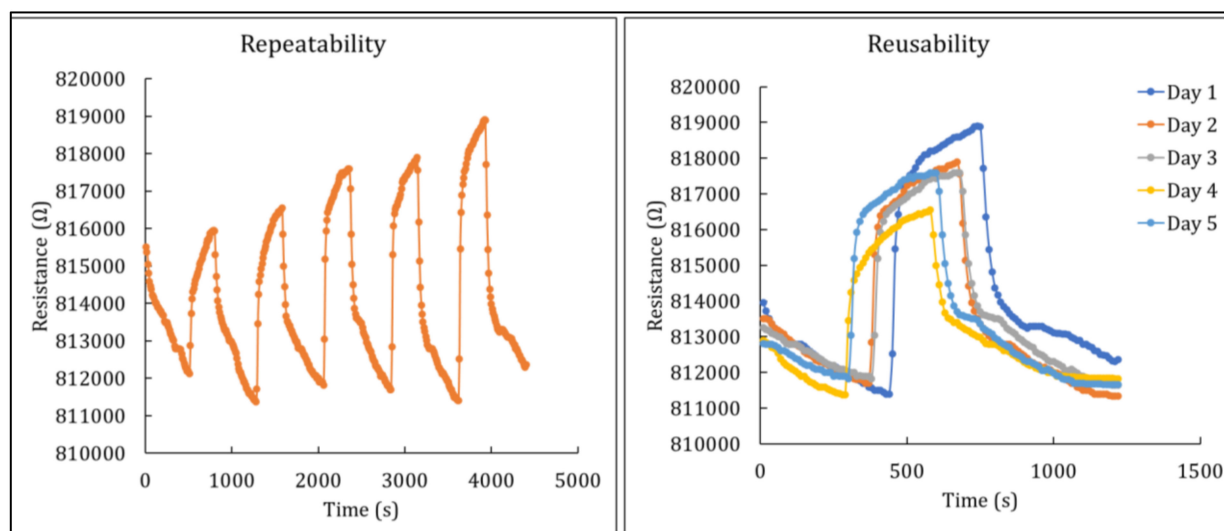
Figure 11. Repeatability and reusability characteristics of nickel ferrite–nanocellulose nanocomposite.

4. Conclusions

Nickel ferrite–nanocellulose nanocomposites could be synthesised using a simple in situ preparation method. In this study of the sensing properties of nickel ferrite, five different weight ratios of nickel ferrite were deposited onto nanocellulose. Nanocomposites exhibited a consistent crystallite size in the nanoscale according to performed XRD measurements. When compared to other weight ratios, 0.3 g nickel ferrite demonstrated improved responsiveness and a shorter recovery time at room temperature. The reaction site in nickel ferrite provided two different cation sites, which promoted high sensitivity in the sensing material. Furthermore, nickel ferrite has a lower reaction barrier compared

to other metals, rendering it highly effective at dissociating chlorine molecules, thereby demonstrating a rapid response to chlorine gas. As such, it has promising future applications for the detection of low concentrations of chlorine gas at room temperature. We aim to continue improving the sensitivity and selectivity of this sensing material in our laboratory. The selectivity of multiple gases using the nanocomposite material can be examined using principal component analysis (PCA). Additionally, the adsorption of various gas analytes on the nanocomposites can be studied by first-principle calculations using density functional theory (DFT). Binding energy, charge transfer, and morphology distance are generally investigated. Hence, electron density analysis could identified that the induction of electron transfer from C atoms in the nanocomposite towards gas analytes leads to the hole (or *p*-type) doping of semiconductor nanocomposites.

Author Contributions: Conceptualization, N.A.M.K., K.K.O. and M.H.Y.; Data curation, N.J. and M.Z.A.; Formal analysis, N.J., M.N.F.N. and M.A.I.A.R.; Funding acquisition, V.F.K.; Investigation, N.A.M.K., M.N.F.N., M.A.I.A.R. and M.H.Y.; Methodology, N.J., M.N.F.N. and M.H.Y.; Project administration, N.A.M.K., S.A.M.N. and W.M.Z.W.Y.; Supervision, N.A.H. and M.Z.A.; Writing—review & editing, V.F.K. All authors have read and agreed to the published version of the manuscript.

Institutional Review Board Statement: Not applicable.

Informed Consent Statement: Not applicable.

Data Availability Statement: The data presented in this study are available on request from the corresponding author.

Conflicts of Interest: The authors declare no conflict of interest.

References

1. Jiang, Y.; McAdam, E.; Zhang, Y.; Heaven, S.; Banks, C.; Longhurst, P. Ammonia inhibition and toxicity in anaerobic digestion: A critical review. *J. Water Process Eng.* **2019**, *32*, 100899. [CrossRef]
2. Al Madhoun, W.; Ramli, N.; Yahaya, A. Monitoring the Total Volatile Organic Compounds (TVOCs) and Benzene Emitted at Different Locations in Malaysia. *J. Eng. Sci.* **2012**, *8*, 61–69.
3. Scholes, C.A.; Stevens, G.W.; Kentish, S.E. The effect of hydrogen sulfide, carbon monoxide and water on the performance of a PDMS membrane in carbon dioxide/nitrogen separation. *J. Membr. Sci.* **2010**, *350*, 189–199. [CrossRef]
4. Li, W.; Zhang, J.; Wang, F.; Qian, L.; Zhou, Y.; Qi, W.; Chen, J. Effect of disinfectant residual on the interaction between bacterial growth and assimilable organic carbon in a drinking water distribution system. *Chemosphere* **2018**, *202*, 586–597. [CrossRef] [PubMed]
5. Wang, H.; Song, T.; Li, Z.; Qiu, J.; Zhao, Y.; Zhang, H.; Wang, J. Exceptional High and Reversible Ammonia Uptake by Two Dimension Few-layer BiI3 Nanosheets. *ACS Appl. Mater. Interfaces* **2021**, *13*, 25918–25925. [CrossRef] [PubMed]
6. Zhang, Z.; Ma, P.; Ahmed, R.; Wang, J.; Akin, D.; Soto, F.; Liu, B.-F.; Li, P.; Demirci, U. Advanced Point-of-Care Testing Technologies for Human Acute Respiratory Virus Detection. *Adv. Mater.* **2022**, *34*, e2103646. [CrossRef]
7. Rafiei, N.; Fatehizadeh, A.; Amin, M.M.; Pourzamani, H.R.; Ebrahimi, A.; Taheri, E.; Aminabhavi, T.M. Application of UV/chlorine processes for the DR83:1 degradation from wastewater: Effect of coexisting anions. *J. Environ. Manag.* **2021**, *297*, 113349. [CrossRef]
8. Wen, G.; Cao, R.; Wan, Q.; Tan, L.; Xu, X.; Wang, J.; Huang, T. Development of fungal spore staining methods for flow cytometric quantification and their application in chlorine-based disinfection. *Chemosphere* **2020**, *243*, 125453. [CrossRef]
9. Kongkaew, S.; Joonyong, K.; Kanatharana, P.; Thavarungkul, P.; Limbut, W. Fabrication and characterization of Prussian blue screen-printed working electrode and their application for free chlorine monitoring in swimming pool water. *Electrochim. Acta* **2021**, *388*, 138558. [CrossRef]
10. Al-Mutlaq, S.; Mahal, E. Amelioration of Bitumen Characteristics Via Natural Rubber Latex and Chlorine Gas. *Egypt. J. Chem.* **2021**, *64*, 2–3. [CrossRef]
11. Liu, J.; Li, T.; Zhang, H.; Zhao, W.; Qu, L.; Chen, S.; Wu, S. Electrospun strong, bioactive, and bioabsorbable silk fibroin/poly (L-lactic-acid) nanoyarns for constructing advanced nanotextile tissue scaffolds. *Mater. Today Bio* **2022**, *14*, 100243. [CrossRef] [PubMed]

12. Arkaban, H.; Khajeh Ebrahimi, A.; Yarahmadi, A.; Zarrintaj, P.; Barani, M. Development of a multifunctional system based on $CoFe_2O_4$@polyacrylic acid NPs conjugated to folic acid and loaded with doxorubicin for cancer theranostics. *Nanotechnology* **2021**, *32*, 305101. [CrossRef] [PubMed]

13. Samal, A.; Honovar, J.; White, C.R.; Patel, R.P. Potential for Chlorine Gas-induced Injury in the Extrapulmonary Vasculature. *Proc. Am. Thorac. Soc.* **2010**, *7*, 290–293. [CrossRef] [PubMed]

14. Gray, N.F. Chapter Thirty-Two—Chlorine Dioxide. In *Microbiology of Waterborne Diseases*, 2nd ed.; Percival, S.L., Yates, M.V., Williams, D.W., Chalmers, R.M., Gray, N.F., Eds.; Academic Press: London, UK, 2014; pp. 591–598; ISBN 978-0-12-415846-7.

15. Zhang, D.; Wu, Z.; Zong, X. Flexible and highly sensitive H_2S gas sensor based on in-situ polymerized SnO_2/rGO/PANI ternary nanocomposite with application in halitosis diagnosis. *Sens. Actuators B Chem.* **2019**, *289*, 32–41. [CrossRef]

16. Singh, G.; Choudhary, A.; Haranath, D.; Joshi, A.G.; Singh, N.; Singh, S.; Pasricha, R. ZnO decorated luminescent graphene as a potential gas sensor at room temperature. *Carbon N. Y.* **2012**, *50*, 385–394. [CrossRef]

17. Bouchikhi, B.; Chludziński, T.; Saidi, T.; Smulko, J.; Bari, N.E.; Wen, H.; Ionescu, R. Formaldehyde detection with chemical gas sensors based on WO_3 nanowires decorated with metal nanoparticles under dark conditions and UV light irradiation. *Sens. Actuators B Chem.* **2020**, *320*, 128331. [CrossRef]

18. Kalidoss, R.; Umapathy, S.; Sivalingam, Y. An investigation of GO-SnO_2-TiO_2 ternary nanocomposite for the detection of acetone in diabetes mellitus patient's breath. *Appl. Surf. Sci.* **2017**, *449*, 677–684. [CrossRef]

19. Behera, B.; Chandra, S. Synthesis of Nanostructured Tungsten Oxide By Thermal Oxidation Method and Its Integration in Sensor for VOCs Detection. *Adv. Mater. Lett.* **2016**, *7*, 697–701. [CrossRef]

20. Tasaltin, C.; Ebeoglu, M.A.; Ozturk, Z.Z. Acoustoelectric effect on the responses of saw sensors coated with electrospun ZnO nanostructured thin film. *Sensors* **2012**, *12*, 12006–12015. [CrossRef]

21. Zhang, L.; Wang, Y.; Ni, Q.Q. Carbon nanotube template-assisted synthesis of zinc ferrite nanochains. *Mater. Chem. Phys.* **2010**, *124*, 1029–1033. [CrossRef]

22. Al-Rawi, N.N.; Anwer, B.A.; Al-Rawi, N.H.; Uthman, A.T.; Ahmed, I.S. Magnetism in drug delivery: The marvels of iron oxides and substituted ferrites nanoparticles. *Saudi Pharm. J.* **2020**, *28*, 876–887. [CrossRef] [PubMed]

23. Chethan, B.; Ravikiran, Y.T.; Vijayakumari, S.C.; Rajprakash, H.G.; Thomas, S. Nickel substituted cadmium ferrite as room temperature operable humidity sensor. *Sens. Actuators A Phys.* **2018**, *280*, 466–474. [CrossRef]

24. Sathisha, I.C.; Manjunatha, K.; Bajorek, A.; Rajesh Babu, B.; Chethan, B.; Ranjeth Kumar Reddy, T.; Ravikiran, Y.T.; Jagadeesha Angadi, V. Enhanced humidity sensing and magnetic properties of bismuth doped copper ferrites for humidity sensor applications. *J. Alloys Compd.* **2020**, *848*, 156577. [CrossRef]

25. Manikandan, V.; Singh, M.; Yadav, B.C.; Mane, R.S.; Vigneselvan, S.; Mirzaei, A.; Chandrasekaran, J. Room temperature LPG sensing properties of tin substituted copper ferrite (Sn−$CuFe_2O_4$) thin film. *Mater. Chem. Phys.* **2020**, *240*, 122265. [CrossRef]

26. Chakraborty, S.; Pal, M. Highly efficient novel carbon monoxide gas sensor based on bismuth ferrite nanoparticles for environmental monitoring. *New J. Chem.* **2018**, *42*, 7188–7196. [CrossRef]

27. Wu, J.; Gao, D.; Sun, T.; Bi, J.; Zhao, Y.; Ning, Z.; Fan, G.; Xie, Z. Highly selective gas sensing properties of partially inversed spinel zinc ferrite towards H_2S. *Sens. Actuators B Chem.* **2016**, *235*, 258–262. [CrossRef]

28. Koli, P.B.; Kapadnis, K.H.; Deshpande, U.G. Nanocrystalline-modified nickel ferrite films: An effective sensor for industrial and environmental gas pollutant detection. *J. Nanostruct. Chem.* **2019**, *9*, 95–110. [CrossRef]

29. Li, Y.; Yuan, Z.; Meng, F. Spinel-type materials used for gas sensing: A review. *Sensors* **2020**, *20*, 5413. [CrossRef]

30. Korotcenkov, G.; Cho, B.K. Metal oxide composites in conductometric gas sensors: Achievements and challenges. *Sens. Actuators B Chem.* **2017**, *244*, 182–210. [CrossRef]

31. Rao, P.; Godbole, R.V.; Bhagwat, S. Chlorine gas sensing performance of palladium doped nickel ferrite thin films. *J. Magn. Magn. Mater.* **2016**, *405*, 219–224. [CrossRef]

32. Sankaran, K.J.; Suman, S.; Sahaw, A.; Balaji, U.; Sakthivel, R. Improved LPG sensing properties of nickel doped cobalt ferrites derived from metallurgical wastes. *J. Magn. Magn. Mater.* **2021**, *537*, 168231. [CrossRef]

33. Manikandan, V.; Kim, J.H.; Mirzaei, A.; Kim, S.S.; Vigneselvan, S.; Singh, M.; Chandrasekaran, J. Effect of temperature on gas sensing properties of lithium (Li) substituted ($NiFe_2O_4$) nickel ferrite thin film. *J. Mol. Struct.* **2019**, *1177*, 485–490. [CrossRef]

34. Reddy, L.P.B.; Prakash, H.G.R.; Ravikiran, Y.T.; Ganiger, S.K.; Angadi, V.J. Structural and humidity sensing properties of niobium pentoxide-mixed nickel ferrite prepared by mechano-chemical mixing method. *J. Mater. Sci. Mater. Electron.* **2020**, *31*, 21981–21999. [CrossRef]

35. Manikandan, V.; Mirzaei, A.; Vigneselvan, S.; Kavita, S.; Mane, R.S.; Kim, S.S.; Chandrasekaran, J. Role of ruthenium in the dielectric, magnetic properties of nickel ferrite (Ru-$NiFe_2O_4$) nanoparticles and their application in hydrogen sensors. *ACS Omega* **2019**, *4*, 12919–12926. [CrossRef]

36. Zhai, C.; Zhang, H.; Du, L.; Wang, D.; Xing, D.; Zhang, M. Nickel/iron-based bimetallic MOF-derived nickel ferrite materials for triethylamine sensing. *Cryst. Eng. Comm.* **2020**, *22*, 1286–1293. [CrossRef]

37. Virlan, C.; Tudorache, F.; Pui, A. Increased sensibility of mixed ferrite humidity sensors by subsequent heat treatment. *Int. J. Appl. Ceram. Technol.* **2017**, *14*, 1174–1182. [CrossRef]

38. Lizundia, E.; Rincón-Iglesias, M.; Lanceros-Méndez, S. Combining cobalt ferrite and graphite with cellulose nanocrystals for magnetically active and electrically conducting mesoporous nanohybrids. *Carbohydr. Polym.* **2020**, *236*, 116001. [CrossRef]

39. Gupta, K.; Kaushik, A.; Tikoo, K.B.; Kumar, V.; Singhal, S. Enhanced catalytic activity of composites of NiFe$_2$O$_4$ and nano cellulose derived from waste biomass for the mitigation of organic pollutants. *Arab. J. Chem.* **2020**, *13*, 783–798. [CrossRef]

40. Fatima, A.; Yasir, S.; Khan, M.S.; Manan, S.; Ullah, M.W.; Ul-Islam, M. Plant extract-loaded bacterial cellulose composite membrane for potential biomedical applications. *J. Bioresour. Bioprod.* **2021**, *6*, 26–32. [CrossRef]

41. Zou, Y.; Zhao, J.; Zhu, J.; Guo, X.; Chen, P.; Duan, G.; Liu, X.; Li, Y. A Mussel-Inspired Polydopamine-Filled Cellulose Aerogel for Solar-Enabled Water Remediation. *ACS Appl. Mater. Interfaces* **2021**, *13*, 7617–7624. [CrossRef]

42. Deeksha, B.; Sadanand, V.; Hariram, N.; Rajulu, A.V. Preparation and properties of cellulose nanocomposite fabrics with in situ generated silver nanoparticles by bioreduction method. *J. Bioresour. Bioprod.* **2021**, *6*, 75–81. [CrossRef]

43. Yang, Y.; Wang, Y.; Zheng, C.; Lin, H.; Xu, R.; Zhu, H.; Bao, L.; Xu, X. Lanthanum carbonate grafted ZSM-5 for superior phosphate uptake: Investigation of the growth and adsorption mechanism. *Chem. Eng. J.* **2022**, *430*, 133166. [CrossRef]

44. Pawar, C.S.; Gujar, M.P.; Mathe, V.L. Synthesis and Characterization of Nano crystalline Nickel Zinc Ferrite for Chlorine * as 6 ensor at 5 oom 7 emperature. *AIP Conf. Proc.* **2015**, *2015*, 050060. [CrossRef]

45. Silva, G.M.G.; Leão, V.N.S.; Pereira, M.F.G.; Faia, P.M.; Araújo, E.S. Zn^{2+}-Doped TiO$_2$:WO$_3$ Films Prepared by Electrospinning and Sintering: Microstructural Characterization and Electrical Signature to Moisture Sensing. *Ceramics* **2021**, *4*, 576–591. [CrossRef]

46. Rahimi Kord Sofla, M.; Brown, R.J.; Tsuzuki, T.; Rainey, T.J. A comparison of cellulose nanocrystals and cellulose nanofibres extracted from bagasse using acid and ball milling methods. *Adv. Nat. Sci. Nanosci. Nanotechnol.* **2016**, *7*, 035004. [CrossRef]

47. Asiri, S.; Sertkol, M.; Güngüneş, H.; Amir, M.; Manikandan, A.; Ercan, I.; Baykal, A. The Temperature Effect on Magnetic Properties of NiFe$_2$O$_4$ Nanoparticles. *J. Inorg. Organomet. Polym. Mater.* **2018**, *28*, 1587–1597. [CrossRef]

48. Virlan, C.; Tudorache, F.; Pui, A. Tertiary NiCuZn ferrites for improved humidity sensors: A systematic study. *Arab. J. Chem.* **2020**, *13*, 2066–2075. [CrossRef]

49. Soleimanpour, A.M.; Jayatissa, A.H.; Sumanasekera, G. Surface and gas sensing properties of nanocrystalline nickel oxide thin films. *Appl. Surf. Sci.* **2013**, *276*, 291–297. [CrossRef]

50. Norrrahim, M.N.F.; Kasim, N.A.M.; Knight, V.F.; Ong, K.K.; Noor, S.A.M.; Halim, N.A.; Shah, N.A.A.; Jamal, S.H.; Janudin, N.; Misenan, M.S.M.; et al. Emerging developments regarding nanocellulose-based membrane filtration material against microbes. *Polymers* **2021**, *13*, 3249. [CrossRef]

51. Sharma, A.K.; Mahajan, A.; Kumar, S.; Debnath, A.K.; Aswal, D.K. Tailoring of the chlorine sensing properties of substituted metal phthalocyanines non-covalently anchored on single-walled carbon nanotubes. *RSC Adv.* **2018**, *8*, 32719–32730. [CrossRef]

52. Šutka, A.; Gross, K.A. Spinel ferrite oxide semiconductor gas sensors. *Sens. Actuators B Chem.* **2016**, *222*, 95–105. [CrossRef]

53. Zhang, W.; Li, Q.; Wang, C.; Ma, J.; Peng, H.; Wen, Y.; Fan, H. High sensitivity and selectivity chlorine gas sensors based on 3D open porous SnO$_2$ synthesized by solid-state method. *Ceram. Int.* **2019**, *45*, 20566–20574. [CrossRef]

54. Bedi, R.K.; Saini, R.; Mahajan, A. Room temperature ppb level chlorine gas sensor based on copper (II) 1,4,8,11,15,18,22,25-octabutoxy-29H,31H-phthalocyanine films. *AIP Conf. Proc.* **2010**, *1313*, 205–208. [CrossRef]

55. Novaro, O.; Pacheco-Blas, M.D.A.; Pacheco-Sánchez, J.H. Potential energy surfaces for reactions of X metal atoms (X = Cu, Zn, Cd, Ga, Al, Au, or Hg) with YH 4 Molecules (Y = C, Si, or Ge) and transition probabilities at avoided crossings in some cases. *Adv. Phys. Chem.* **2012**, *2012*, 720197. [CrossRef]

56. Gao, Z.; Wang, C.; Gao, N.; Guo, S.; Chen, Y.; Chai, Z.; Wang, Y.; Ma, H. Electrodeposited Ni-W coatings as the effective reaction barrier at Ga-21.5In-10Sn/Cu interfaces. *Surf. Interfaces* **2022**, *30*, 101838. [CrossRef]

57. Li, Y.; Zhou, X.; Hu, J.; Zheng, Y.; Huang, M.; Guo, K.; Li, C. Reversible Mg metal anode in conventional electrolyte enabled by durable heterogeneous SEI with low surface diffusion barrier. *Energy Storage Mater.* **2022**, *46*, 1–9. [CrossRef]

58. Rák, Z.; Brenner, D.W. Negative surface energies of nickel ferrite nanoparticles under hydrothermal conditions. *J. Nanomater.* **2019**, *2019*, 5268415. [CrossRef]

59. Kamble, R.B.; Mathe, V.L. Nanocrystalline nickel ferrite thick film as an efficient gas sensor at room temperature. *Sens. Actuators B Chem.* **2008**, *131*, 205–209. [CrossRef]